lubricants

MDPI

Article

Nonlinear Dynamic Responses of Rigid Rotor Supported by Thick Top Foil Bearings

Bin Hu [1], Xiaodong Yang [2,*], Anping Hou [1], Rui Wang [1], Zhiyong Wu [3], Qifeng Ni [4] and Zhong Li [5]

[1] School of Energy and Power Engineering, Beihang University, Beijing 100191, China; bh1204hb@163.com (B.H.); houap@buaa.edu.cn (A.H.); wangrbuaa@126.com (R.W.)
[2] Institute of Artificial Intelligence, Beihang University, Beijing 100191, China
[3] The Key Laboratory of Solar Thermal Energy and Photovoltaic System, Institute of Electrical Engineering, Chinese Academy of Sciences (IEE-CAS), Beijing 100190, China; wuzhiyong@mail.iee.ac.cn
[4] Ningbo Hudu Energy Technology Co., Ltd., Ningbo 315000, China; nqf888@163.com
[5] Zhengzhou Aerotropolis Institute of Artificial Intelligence, Zhengzhou 451162, China; 17888821559@163.com
* Correspondence: yangxiaodong@buaa.edu.cn

Abstract: This study focuses on thick top foil bearings (TTFBs), which can prevent top foil from sagging and significantly reduce the load capacity of gas foil bearings (GFBs). However, the limited research on the dynamic responses of TTFB-rotor systems has hindered their wide application of TTFBs with high load capacity. To address this, an integrated nonlinear dynamic model is developed to analyze the linear dynamic responses of a rigid rotor supported on TTFBs. The model incorporates time domain orbit simulation, considering unsteady Reynolds equations, foil deformation equations, thick top foil motion equations, and rotor motion equations. A symmetrical test rig is used to validate the model, and three types of TTFBs with different bump foil stiffness are tested, with experimental results aligning with the model predictions. This study also investigates the effects of nominal clearance, static load, and unbalance on TTFB-rotor systems. The results indicate that unbalance has minimal impact on subsynchronous vibrations. However, larger bump foil stiffness, increased normal clearance, and higher static load contribute to improved stability and higher maximum stable speed of the TTFB-rotor system. Moreover, other relevant parameters reducing the bearing attitude angle can further enhance the system's stability.

Keywords: nonlinear numerical prediction; thick top foil; subsynchronous vibrations; experimental investigation

Citation: Hu, B.; Yang, X.; Hou, A.; Wang, R.; Wu, Z.; Ni, Q.; Li, Z. Nonlinear Dynamic Responses of Rigid Rotor Supported by Thick Top Foil Bearings. *Lubricants* **2023**, *11*, 453. https://doi.org/10.3390/lubricants11100453

Received: 12 September 2023
Revised: 2 October 2023
Accepted: 12 October 2023
Published: 20 October 2023

1. Introduction

Increasing the rotational speed of rotating machinery can significantly improve energy density and efficiency. Gas foil bearings (GFBs) are oil-free bearings that meet the high-speed requirement due to their low friction and high DN (shaft diameter in millimeters multiplied by shaft rotational speed in rev/min) limit [1–3]. In contrast with traditional oil-lubricated bearings, GFBs eliminate the need for an oil-lubrication system, resulting in a compact structure and reduced energy loss [4,5]. These advantageous characteristics have greatly facilitated the successful application of GFBs in high-speed turbomachinery systems, including cryogenic turboexpanders, Brayton air refrigerator systems, high-speed machining centers, and micro-power generator systems [6–9].

However, GFB-rotor systems often experience severe subsynchronous vibrations at high rotating speeds, limiting the range of their applications [10]. As a result, numerous studies have focused on investigating the dynamic responses of GFB-rotor systems. Several researchers have used a perturbation method to calculate the dynamic stiffness and damping coefficients for analyzing the dynamic responses of GFB-rotor systems. Ku et al. [11] introduced this method to predict the structural stiffness and damping of foil when a rotor is in its static equilibrium position. Lee et al. [12] compared the dynamic responses of a

super-critical rotor supported by conventional bump foil bearings and viscoelastic bearings using experimental and theoretical results. The theoretical orbit calculations, based on dynamic stiffness and damping coefficients, showed a good agreement with the experimental results when the vibration amplitude of the rotating speed remained below the bending critical speed. The theoretical findings indicated that enhancing the structural damping of the foil structure reduced vibration. Vleugels et al. [13] conducted a stability analysis of the GFB-rotor system using dynamic stiffness and damping coefficients. They assumed the foil structure acted as a uniform elastic foundation to calculate the dynamic stiffness and damping properties. Numerical results indicated that bearing compliance significantly influenced the dynamic stiffness, and increasing the bearing load and reducing the ratio of the nominal bearing clearance to the rotor radius enhanced stability. Kim et al. [14] performed theoretical and experimental research on the effects of mechanical preload. Metal shims were inserted beneath the bump-strip layers of shimmed GFBs to introduce mechanical preload. Compared with the original GFBs, the shimmed GFBs exhibited a noticeable increase in dynamic direct stiffness and direct damping. The multiple lobe film clearance profile created by the metal shims reduced the amplitude of subsynchronous whirl motions and increased the natural frequency of the GFB-rotor system, as confirmed by experimental results. Theoretical and experimental results also indicated that rotor unbalance and the gas film had a significant influence on nonlinear dynamic responses, although the foil structure was simplified as a uniform elastic foundation with a given value. Xu et al. [15] developed a more comprehensive GFB model that considered nonlinearity in the foil structure to predict dynamic responses in GFB-rotor systems. They calculated dynamic stiffness and damping coefficients based on a quadratic bump stiffness model derived from experimental bearing stiffness data. The simulation results of the quadratic bump stiffness model differed significantly from those of the linear bump stiffness model, indicating the significant impact of foil structure nonlinearity on the dynamic responses of GFB-rotor systems. Hoffmann et al. [16] used a link-spring model incorporating frictional contacts and bump interactions to investigate the nonlinear vibrations of GFB-rotor systems. Using experimental and numerical testing of two contrasting cases with different balanced rotors, they identified the source of subsynchronous vibrations. The simulation results showed good agreement with the measurements, indicating that interaction between the gas film and the rotor caused subsynchronous vibrations when unbalance was significant. When unbalance was minor, the subsynchronous vibrations originated from the self-excitation of the gas film.

However, the dynamic stiffness and damping coefficients were perturbation results calculated using linearized Reynolds equations when the rotor displacements were small relative to its static equilibrium position. Subsynchronous vibrations with large amplitudes were common in many tests, highlighting the limitations of the linear perturbation approach. Kim [17] investigated the dynamic responses of GFB-rotor systems using both linear and nonlinear approaches. It was found that the rotor–bearing natural frequencies predicted using the two approaches were similar. However, the onset speeds of instability differed significantly between the time domain nonlinear orbit simulations and the linear stability simulations based on the dynamic stiffness and damping coefficients. Bou et al. [18] conducted a comparison between a nonlinear time-dependent approach and the classical linear approach using dynamic stiffness and damping coefficients. The classical linear approach was found to have a valid range of relative eccentricity lower than 0.65. For high values of eccentricity, the accuracy of the results required the use of the nonlinear approach. Larsen et al. [19] also compared the two approaches for predicting the onset speed of instability. It was observed that the classical linear approach was only suitable when the uniform foil stiffness was high and the load was small. When the uniform foil stiffness was reduced or the load level was increased, there were significant discrepancies in the prediction of the onset speed of instability. The nonlinear time domain approach, however, could accurately predict the actual rotor response, which the classical linear approach was unable to achieve. Consequently, many researchers have adopted nonlinear

analysis approaches. Bhore et al. [20] proposed a nonlinear time domain orbit simulation that coupled the equations of the unsteady Reynolds equation, foil deformation, and rotor motion. They conducted parametric studies on rotating speed, unbalance eccentricity, compliance, and the loss factor, revealing highly nonlinear behaviors of the disc and journal center motion. However, the foil structure was simplified as a uniform elastic foundation. Larsen et al. [21] studied the effect of unbalance and rotational speed using theoretical modeling and experimental testing. The theoretical results, solved with a mathematical approach in the time domain, showed good agreement with the experimental results. Both the theoretical and experimental results indicated that subsynchronous vibrations were primarily influenced by unbalance and rotational speed. Additionally, the correct estimation of the foil stiffness and loss factor significantly affected the accuracy of the predictions. Osmanski et al. [22] proposed a new foil model based on truss representation, considering foil mass and frictional energy dissipation at foil interfaces. They presented a nonlinear time domain model to calculate the dynamic responses of GFB-rotor systems using this foil model. The simulation results showed good agreement with the experimental results, suggesting that the natural frequencies and mode shapes were accurately captured. Bonello et al. [23] introduced a modal-based bump foil model that considered the dynamic interaction between bumps and their inertia. They used a simultaneous solution technique to integrate the rotor, gas film, and foil domains into a coupled dynamical system model. This approach accurately predicted the nonlinear behaviors of GFB-rotor systems. The imposition of pressure constraints on the gas film delayed the onset speed of instability, aligning well with experimental results. Moreover, the significant influence of gas film non-linearity on the non-linear behaviors of GFB-rotor systems was verified with measured and predicted nonlinear phenomena. The aforementioned studies demonstrate that nonlinear analysis approaches yield more accurate dynamic responses of GFB-rotor systems.

Most recently, a type of bump-type foil bearing with a thick top foil was introduced to handle heavy load conditions [24,25]. In comparison with traditional gas foil bearings (GFBs) with thin top foils, TTFBs showed significant improvements in load capacity by reducing the sagging of the top foil, as depicted in Figure 1. Wang et al. [24] developed a theoretical model for a TTFB and predicted its load capacity and dynamic force coefficients. The numerical results indicated a 23% increase in load capacity compared with a GFB, along with different dynamic force coefficients. However, the numerical results were not experimentally validated. Li et al. [25] developed a three-dimensional finite element model based on contact mechanics to investigate the load capacity of TTFBs. The numerical results, which agreed well with experimental findings, demonstrated a 100% improvement in load capacity compared with GFBs with thin top foils. The thickness of the top foil was found to have a significant impact on the degree of sagging and bearing stiffness. However, the study primarily focused on load capacity, and there is currently a lack of research on the dynamic responses of TTFB-rotor systems. This knowledge gap severely hinders the application and wider adoption of TTFBs, despite their high load capacity.

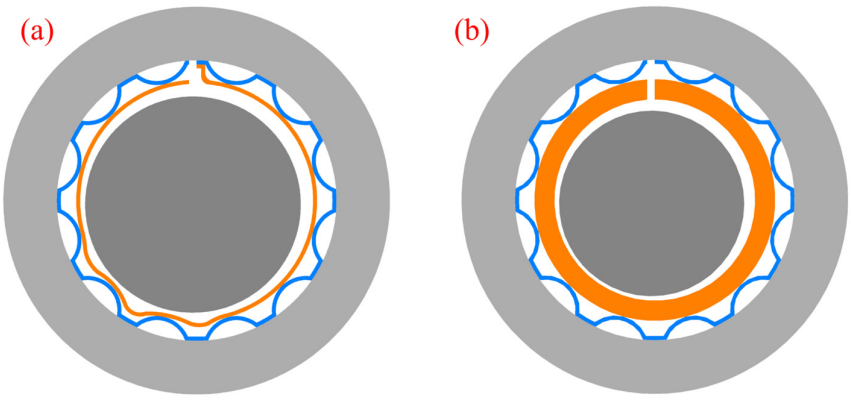

Figure 1. Schematic view of (**a**) a GFB with thin top foil and (**b**) a TTFB [25].

This paper presents an integrated nonlinear dynamic model for investigating the dynamic responses of TTFB-rotor systems, where a rigid rotor is supported by TTFBs. The model consists of a time-domain orbit simulation that couples unsteady Reynolds equations, foil deformation equations, thick top foil motion equations, and rotor motion equations. To validate the simulation results, various bump foil stiffness scenarios are tested against data obtained from a symmetrical test rig. The analysis of dynamic responses uses fast Fourier transform (FFT), waterfall plots, orbit simulations, and Poincaré maps. The simulation considers the impact of parameters such as nominal clearance, static load, and unbalance on the nonlinear responses of the TTFB-rotor system. By carefully selecting these parameters, a deeper understanding of the TTFB-rotor system is obtained. Furthermore, the obtained results and discussions are of importance to promote the application of TTFBs in high-speed and high-performance rotating machinery systems.

2. Nonlinear Numerical Prediction Method

The nonlinear model of the GFB-rotor system is typically divided into three components: the shaft part, which is based on rotor motion equations; the gas film part, which is based on unsteady Reynolds equations; and the bump structure part, which is based on foil deformation equations, as depicted in Figure 2a [26]. However, in the case of the TTFB-rotor system, the weight of the thick top foil needs to be considered. The thick top foil has a thickness of 1.5~2.0 mm, which is significantly thicker than the thin top foil's 0.1~0.2 mm. As a result, the thick top foil part should be added as the fourth component to the TTFB-rotor system, as shown in Figure 2b. A time-domain orbit simulation is conducted, integrating these four components, to accurately simulate the performance of the TTFB-rotor system.

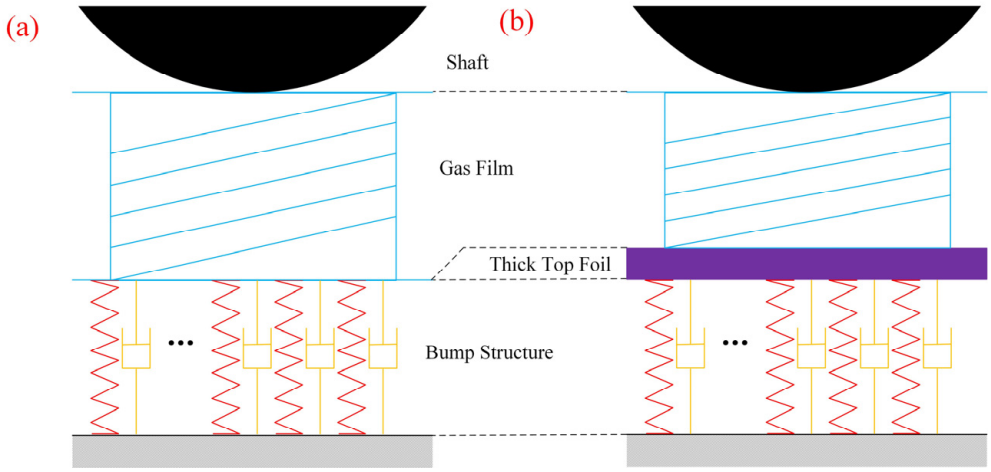

Figure 2. Schematic view of (**a**) GFB-rotor [26] and (**b**) TTFB-rotor system models.

2.1. Theoretical Model for TTFB

As shown in Figure 3, the theoretical model of a TTFB is composed of a gas film part based on unsteady Reynolds equations, a bump structure part based on foil deformation equations, and a thick top foil part based on motion equations of the thick top foil. The dimensionless transient compressible Reynolds equation that calculates the dynamic pressure and film thickness distribution of a TTFB is written as

$$\frac{\partial}{\partial\theta}\left(P_d H^3 \frac{\partial P_d}{\partial\theta}\right) + \frac{\partial}{\partial Z}\left(P_d H^3 \frac{\partial P_d}{\partial Z}\right) = \Lambda \frac{\partial}{\partial\theta}(P_d H) + 2\Lambda\gamma \frac{\partial}{\partial T}(P_d H) \quad (1)$$

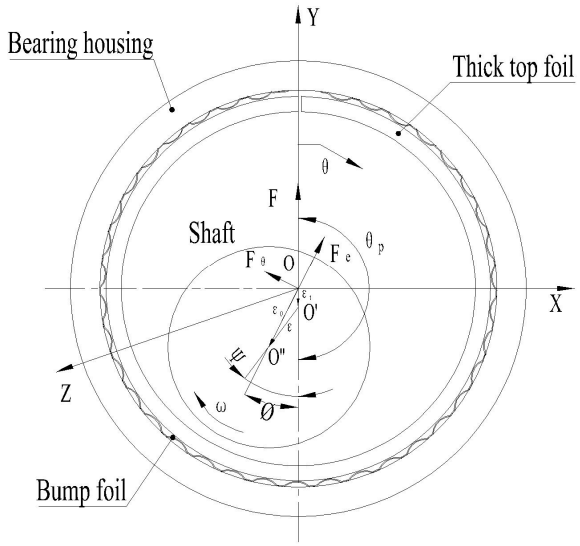

Figure 3. Coordinate system of a TTFB.

The dimensionless bearing axial width Z, pressure P_d, gas film thickness H, bearing number Λ, excitation frequency ratio γ, and time T in Equation (1) are written in Equation (2) as

$$Z = \frac{z}{R}, \quad P_d = \frac{p}{p_a}, \quad H = \frac{h}{C_0}, \quad \Lambda = \frac{6\mu\omega}{p_a} \cdot \left(\frac{R}{C_0}\right)^2, \quad \gamma = \frac{\omega_e}{\omega}, \quad T = \omega_e t \tag{2}$$

where the bearing radius R ambient pressure p_a, nominal clearance C_0, viscosity of gas μ, rotational frequency ω, excitation frequency ω_e, and time t are used in the dimensionless representation of the above-mentioned parameters.

Based on the structural characteristics of TTFBs, both the displacement of the rotor and the movement of the thick top foil dominate the eccentricity of a TTFB. Therefore, the eccentricity vector of a TTFB is the relative eccentricity vector ε obtained by subtracting the eccentricity vector of the rotor and the eccentricity vector of the thick top foil. The unsteady gas film thickness is written as

$$H = \frac{h}{C_0} = 1 + |\vec{\varepsilon}| \cos(\theta - \Psi) \tag{3}$$

where $|\vec{\varepsilon}|$ and Ψ are the modulus and angle of the relative eccentricity vector ε, respectively. In Equation (3), the term of the bump deflection is not included for the thick top foil is assumed as the rigid body [24].

The dimensionless transient compressible Reynolds equation is solved using the alternating-direction implicit method. When the transient gas film pressure field meets the condition of convergence, the pressure field is integrated using Simpson's one-third rule to calculate transient TTFB hydrodynamic film force in the x- and y-directions. The force is written as

$$F_{TTFB,x} = -\int_{-\frac{L}{2R}}^{\frac{L}{2R}} \int_0^{2\pi} (P_d(\theta, Z) - 1) \sin\theta d\theta dZ \tag{4}$$

$$F_{TTFB,y} = -\int_{-\frac{L}{2R}}^{\frac{L}{2R}} \int_0^{2\pi} (P_d(\theta, Z) - 1) \cos\theta d\theta dZ \tag{5}$$

The weight of the thick top foil is no longer small compared with that of the rotor; thus, it should be taken into account. The motion equation of the thick top foil is written as

$$m_{TF}\ddot{e}_{TF,x} + c_x\dot{e}_{TF,x} + k_x e_{TF,x} + F_{TTFB,x} = 0 \tag{6}$$

$$m_{TF}\ddot{e}_{TF,y} + c_y\dot{e}_{TF,y} + k_y e_{TF,y} + F_{TTFB,y} = 0 \tag{7}$$

where $e_{TF,x}$ and $e_{TF,y}$, k_x and k_y, and c_x and c_y are the displacement, stiffness, damping of the thick top foil in the x- and y-directions, respectively.

k_x and k_y are the combined stiffness of the deformed bumps in the x- and y-directions, they can be written as

$$\begin{cases} k_x = \sum_{j=1}^{n} k_j \sin^2(\phi_j - \theta_p) \\ k_y = \sum_{j=1}^{n} k_j \cos^2(\phi_j - \theta_p) \end{cases} \tag{8}$$

where k_j is the stiffness of the JTH deformed bump and ϕ_j is the angle of the JTH deformed bump. In this paper, k_j is derived on the basis of the model with linear stiffness distribution [27].

c_x and c_y are the combined damping of the deformed bumps in the x- and y-directions, they can be written as

$$\begin{cases} c_x = \eta k_x/\omega \\ c_y = \eta k_y/\omega \end{cases} \tag{9}$$

where η is foil structural loss factor [20].

2.2. Theoretical Model for the Rigid Rotor

The structure of the TTFB-rotor system, as depicted in Figure 4, was investigated in this study. Unbalance was added symmetrically to the shaft, and the eddy current probe was positioned symmetrically for measurement. The shaft was divided into 20 beam elements with 80 degrees of freedom, utilizing a beam model based on the finite element method (FEM). The thrust disks and turbines mounted on the shaft were treated as beam elements and the Timoshenko beam theory was used to account for the shear effect. The nonlinear bearing forces were represented as concentrated forces at the centers of each thick top foil.

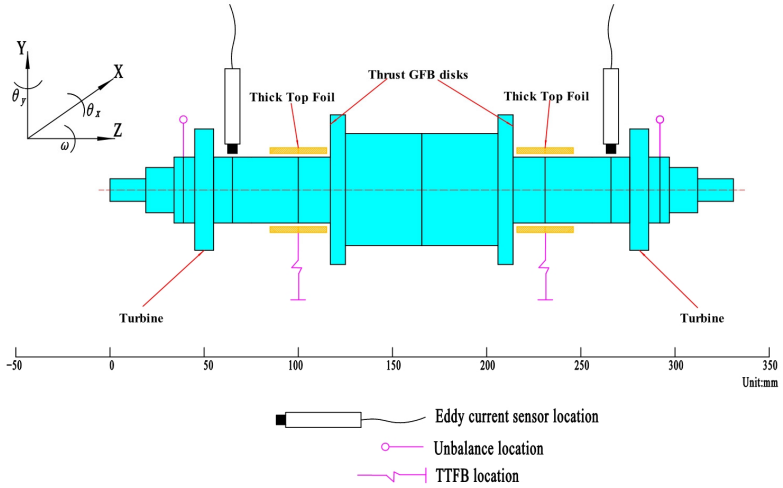

Figure 4. Schematic of the TTFB-rotor system.

When adopting the assumptions described above, the motion equation of the shaft is written as

$$M_J\ddot{e}_J + [C_J + \omega G]\dot{e}_J + K_J e_J = F_{TTFB} + F_g + F_u \tag{10}$$

where $(e_J)_i = [x_i \quad y_j \quad \theta_{xi} \quad \theta_{yi}]^T$ is the displacement of each node at the shaft, x_i, y_i and θ_{xi}, θ_{yi} are the lateral and rotational displacements, respectively. M_J, C_J, G, and M_J are the mass, damping, gyroscopic, and stiffness matrixes. The damping effect of the system is

considered to be related only to the nonlinear bearing force; therefore, the damping matrix C_J is set to zero [26]. F_{TTFB} is the nonlinear TTFB force vector, and F_g is the gravity force vector. F_u is the force vector induced by the unbalance, and F_u of each node at the shaft is written as

$$F_u(t) = \begin{bmatrix} F_{ux}(t) \\ F_{uy}(t) \\ M_{ux}(t) \\ M_{uy}(t) \end{bmatrix} = \omega^2 \begin{Bmatrix} m_u r_u \cos(\omega t) \\ m_u r_u \sin(\omega t) \\ 0 \\ 0 \end{Bmatrix} \tag{11}$$

where F_{ux} and F_{uy} are the unbalance force in the horizontal and vertical directions, whereas the unbalance moments M_{ux} and M_{uy} are set to zero [26]. m_u is the unbalance mass of the shaft, and r_u is the radius of the unbalance mass.

2.3. Orbit Simulation

A time-domain orbit simulation coupling unsteady Reynolds equations, foil deformation equations, thick top foil motion equations, and rotor motion equations is conducted to analyze the nonlinear dynamic responses.

Equations (6), (7) and (10) are nonlinear equations. Two kinds of numerical calculation methods, one being the explicit time history method and the other being the implicit time history method, can be adopted to solve them [28]. The Newmark method selected in this paper is an implicit time history method. The Newmark method is a method for modifying linear acceleration. By introducing two parameters α and β into the velocity and displacement expressions at time $t + \Delta t$, two basic equations of the Newmark method can be written as

$$\{\dot{u}(t+\Delta t)\} = \{\dot{u}(t)\} + [(1-\alpha)\{\ddot{u}(t)\} + \alpha\{\ddot{u}(t+\Delta t)\}] \times \Delta t \tag{12}$$

$$\{u(t+\Delta t)\} = \{u(t)\} + \{\dot{u}(t)\} \times \Delta t + \left[\left(\frac{1}{2} - \beta\right)\{\ddot{u}(t)\} + \beta\{\ddot{u}(t+\Delta t)\}\right] \times \Delta t^2 \tag{13}$$

In the Newmark method, the control parameters α and β affect the accuracy and stability of the whole algorithm. Only when $\alpha = 0.5$ and $\beta = 0.25$, the Newmark method has second-order accuracy and unconditional stability. Therefore, the control parameters α and β are assigned as 0.5 and 0.25, respectively, in research and engineering applications. The Newmark method is called the constant mean acceleration method. Equations (12) and (13) are transformed into

$$\{\dot{u}(t+\Delta t)\} = \{\dot{u}(t)\} + \frac{1}{2}(\{\ddot{u}(t)\} + \{\ddot{u}(t+\Delta t)\}) \times \Delta t \tag{14}$$

$$\{u(t+\Delta t)\} = \{u(t)\} + \{\dot{u}(t)\} \times \Delta t + \left[\frac{1}{4}(\{\ddot{u}(t)\} + \{\ddot{u}(t+\Delta t)\})\right] \times \Delta t^2 \tag{15}$$

Accordingly, the constant average acceleration method is used in this paper to calculate the trajectory of the rigid rotor and the thick top foil.

For the shaft, the dynamic response at time $n+1$ is calculated using

$$\dot{e}_J^{n+1} = \dot{e}_J^n + \frac{1}{2}\left(\ddot{e}_J^n + \ddot{e}_J^n\right) \tag{16}$$

$$e_J^{n+1} = e_J^n + \dot{e}_J^n \times \Delta t + \frac{1}{4}\left(\ddot{e}_J^n + \ddot{e}_J^n\right) \times (\Delta t)^2 \tag{17}$$

For the thick top foil, the dynamic response at time $n+1$ is calculated using

$$\hat{k} = k^n + 4\frac{m_{TF}}{(\Delta t)^2} + 2\frac{c^n}{\Delta t} \tag{18}$$

$$\hat{p}^{n+1} = -F_{film}^{n+1} + \left(4\frac{e_{TF}^{n}}{(\Delta t)^2} + 4\frac{\dot{e}_{TF}^{n}}{\Delta t} + \ddot{e}_{TF}^{n}\right)m_{TF} + \left(2\frac{e_{TF}^{n}}{\Delta t} + \dot{e}_{TF}^{n}\right)c^{n} \tag{19}$$

$$e_{TF}^{n+1} = \hat{P}^{n+1}/\hat{k} \tag{20}$$

$$\ddot{e}_{TF}^{n+1} = 4\frac{e_{TF}^{n+1} - e_{TF}^{n}}{(\Delta t)^2} - 4\frac{\dot{e}_{TF}^{n}}{\Delta t} - \ddot{e}_{TF}^{n} \tag{21}$$

$$\dot{e}_{TF}^{n+1} = \dot{e}_{TF}^{n} + \frac{1}{2}\left(\ddot{e}_{TF}^{n} + \ddot{e}_{TF}^{n+1}\right)\Delta t \tag{22}$$

In the TTFB-rotor system, the compressible transient Reynolds equation used to solve the gas film transient pressure distribution is a second-order partial differential equation, and the dynamic equation used to solve the rotor and thick top foil trajectory is a second-order ordinary differential equation. In the process of solving the rotor trajectory, in each time step, these two equations need to be solved simultaneously. However, in the process of solving these two equations, the results of the other side are required as the initial conditions, so the synchronous coupling solution is difficult to carry out. In order to predict the nonlinear dynamic characteristics of the TTFB-rotor system, a linear displacement prediction method is used to solve the synchronous coupling problem [28]. The linear displacement prediction method assumes that the displacement of the thick top foil and rotor changes linearly at step $n-1$, step n, and step $n+1$, and can be written as

$$\frac{e_{J(predict)}^{n+1} - e_{J}^{n}}{\Delta t} = \frac{e_{J}^{n} - e_{J}^{n-1}}{\Delta t} \tag{23}$$

$$\frac{e_{TF(predict)}^{n+1} - e_{TF}^{n}}{\Delta t} = \frac{e_{TF}^{n} - e_{TF}^{n-1}}{\Delta t} \tag{24}$$

According to Equations (23) and (24), based on the thick top foil and axial diameter displacement of step $n-1$ and step n, the gas film thickness of step $n+1$ can be predicted as

$$H_{predict}^{n+1} = 1 - \frac{2e_{J,x}^{n} - e_{J,x}^{n-1}}{C_0}cos\theta - \frac{2e_{J,y}^{n} - e_{J,y}^{n-1}}{C_0}sin\theta + \frac{2e_{TF,x}^{n} - e_{TF,x}^{n-1}}{C_0}cos\theta + \frac{2e_{TF,y}^{n} - e_{TF,y}^{n-1}}{C_0}sin\theta \tag{25}$$

To provide a referable analysis, 50 time steps are calculated per revolution to solve the rotor orbit. The steady-state solutions for each rotational speed are carried out to simulate the entire TTFB-rotor system speed-up test because unsteady-state solutions are very time-consuming.

3. Model Verification

To validate the method for predicting subsynchronous responses in the TTFB-rotor system, an experimental setup is designed and conducted. The TTFB used in the test is illustrated in Figure 5 and consists of a thick top foil, bump foil, bearing housing, and snap ring. The displacement of the thick top foil in the circumferential direction is restricted by inserting lugs into the grooves of the snap ring and bearing housing. In the axial direction, the displacement of the thick top foil is limited by the snap ring and the internal end face of the bearing housing. The configuration of the test rig is shown in Figure 6. A symmetric design is used for the rotor, which comprises two identical impulse turbines to ensure that both TTFBs bear the same load. A pair of gas foil thrust bearings is utilized to limit axial movement of the rotor. Four eddy current sensors are used to measure the radial displacement of the TTFBs, while a laser speed sensor tracks the rotor's speed and phase. The dimensions of the two test TTFBs are as follows: a radius of 17.56 mm and a width of 30 mm. The impulse turbine tip clearance is set at 0.3 mm, ensuring that the rotor has sufficient torque to lift off and reach a maximum speed of 60 krpm under an

inlet compressed air pressure of 0.7 Mpa. All data are acquired using a dynamic signal acquisition system developed by Donghua. The shaft weight is 4 kg, resulting in a static load of 2 kg on each bearing. Both TTFBs undergo the same manufacturing process, heat treatment, and assembly. The inner diameter of the TTFBs is measured with a micrometer gauge as shown in Figure 7, and the diameter of the shaft is measured with an outside micrometer. The value of the nominal clearance is obtained by subtracting the radius of the TTFBs from the radius of the shaft. In this paper, a nominal clearance of 60 µm was tested. The thick top foil has a thickness of 1.5 mm and is coated with a 20 µm thickness of PTFE to prevent potential wear on both the TTFBs and the shaft. The rotor unbalance is reduced to a G1.0 level using a commercial dynamic balancer. Scribed lines are marked to ensure that the unbalance amount of the rotor remains unchanged after disassembly and reassembly. Table 1 provides a detailed overview of the physical and geometric parameters of the TTFB-rotor system.

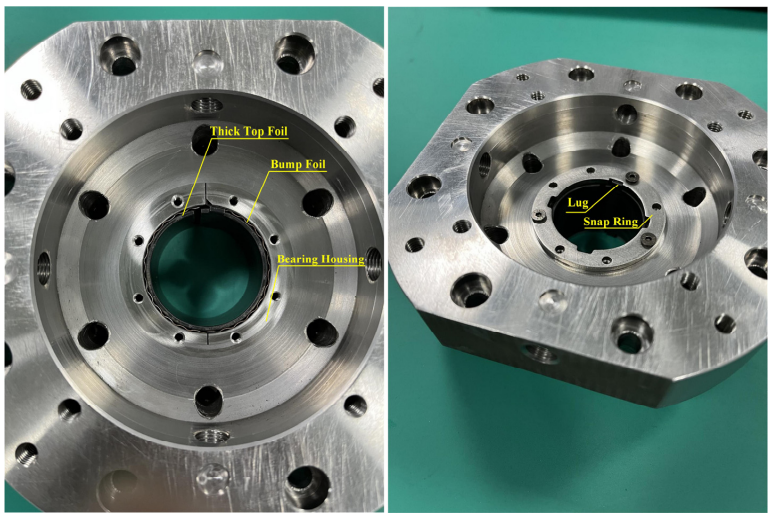

Figure 5. A photo of test TTFBs.

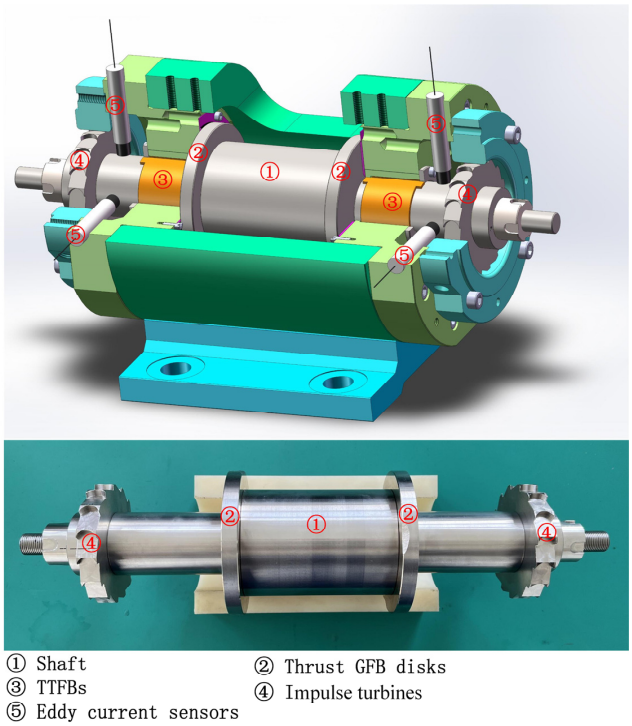

Figure 6. Schematic of the test TTFB-rotor system.

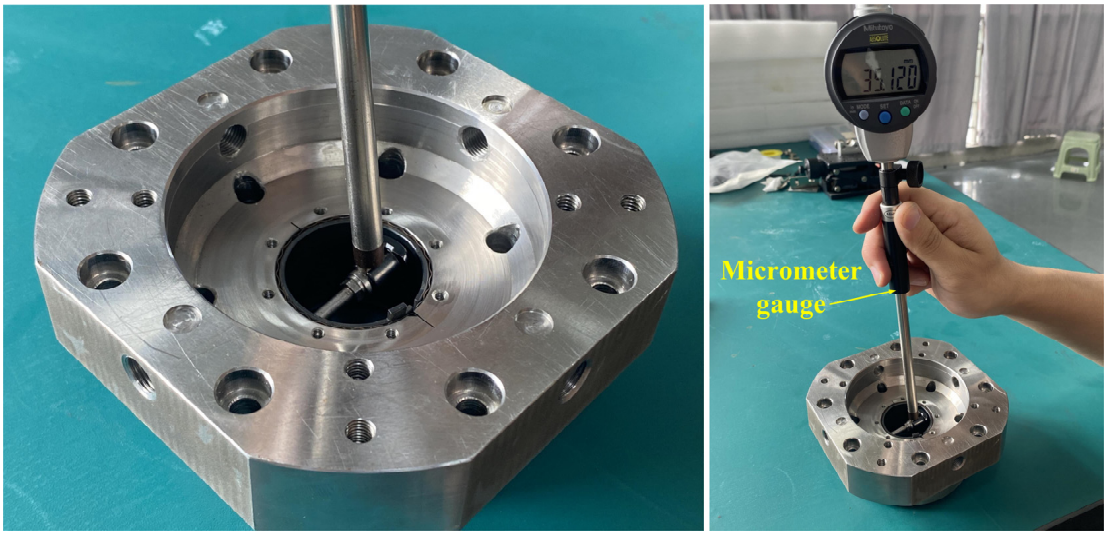

Figure 7. A photo of measuring the inner diameter of test TTFBs.

Table 1. Physical and geometric parameters of the TTFB-rotor system.

TTFB Parameters	
Bearing radius	17.56 mm
Bearing axial width	30 mm
Thick top foil thickness	1.5 mm
Thick top foil mass	0.041 kg
Bump material	3J1
Bump foil thickness	0.1 mm
Bump half length	1.25 mm
Bump height	0.51 mm
Number of bumps	38
Young's modulus	186 Gpa
Poisson's ratio	0.29
Gas viscosity	1.81×10^{-5} Pa·s
GFTB parameters	
Bearing inner radius	20 mm
Bearing outer radius	40 mm
Top foil angle (six pads)	58°
Inclined plane angle	30°
Foil thickness	0.1 mm
Rotor parameters	
Total mass	4 kg
Unbalance	4 g·mm
Radius at bearing location	17.5 mm
Total length	331 mm
Young's modulus	210 Gpa
Material density	7800 kg·m^{-3}

The maximum stable speed is achieved by accelerating the rotational speed using two symmetrically identical impulse turbines. During orbit simulations, a stable limit cycle cannot form beyond the maximum stable speed. In the experiment, when the maximum stable speed is exceeded, there is a noticeable sound of abnormal collision between the shaft and the thick top foil. To mitigate the impact of additional vibrations near the critical speed, a modal analysis of the rotor is performed, and the resulting Campbell diagram plot is presented in Figure 8. The first-order forward and backward whirling frequencies are 2247 Hz and 1999 Hz, respectively. Due to the symmetrical structure of the test rig, the

vibrations on the left and right sides are similar. For research convenience, the vibration signals in the vertical direction at the right end are uniformly analyzed. Figure 9 illustrates that synchronous vibrations, marked as 1X and characterized by a frequency equal to the rotational frequency, are present. The amplitude of synchronous vibrations remains stable as the rotational speed changes, with simulation and experimental steady values of 0.88 μm and 1.21 μm, respectively. Subsynchronous vibrations, on the other hand, maintain a frequency that does not vary with the rotational speed. As the rotational speed increases, the simulation amplitude of subsynchronous vibrations also increases, and the increase becomes more pronounced as the rotational speed approaches the maximum stable speed. The experimental results exhibit a similar trend. Using ten-order zero-phase digital band pass filters [29], Figure 10 also illustrates that as the rotational speed increases, the simulation results and experimental results exhibit more pronounced subsynchronous vibrations. The predicted frequency and peak amplitude of the subsynchronous vibrations are 99 Hz and 9.12 μm, respectively, closely matching the corresponding experimental results of 102 Hz and 10.30 μm. The predicted and experimental maximum stable speeds are also close, with values of 36 krpm and 35.58 krpm, respectively. Comparing the simulation results with the experimental results, it is evident that both synchronous and subsynchronous vibrations are well-matched between the two.

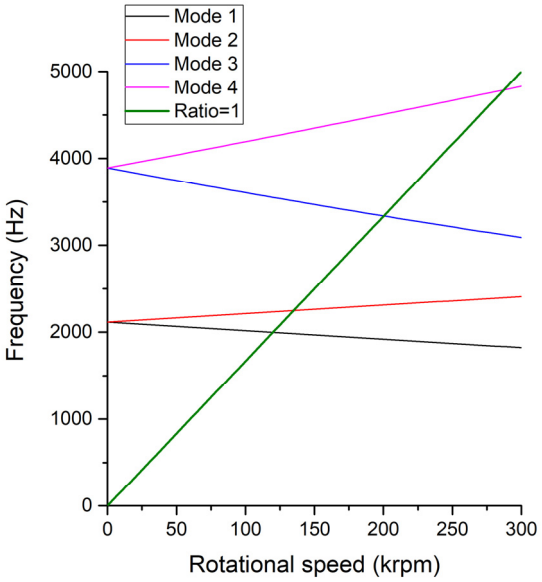

Figure 8. Campbell diagram plot of the rotor.

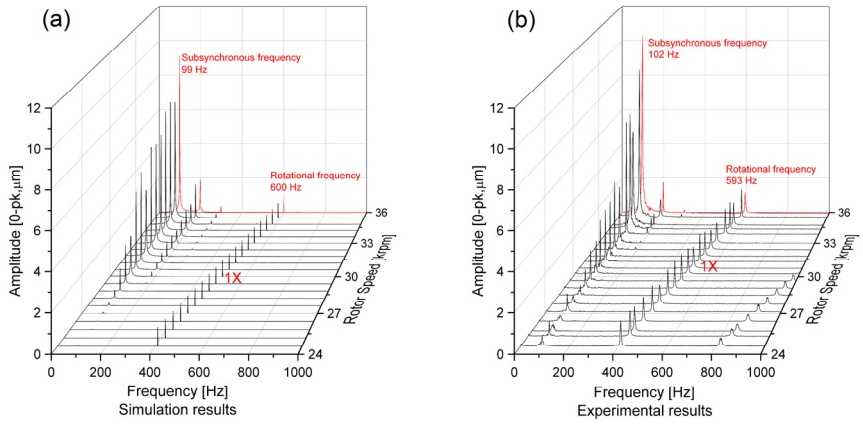

Figure 9. Waterfall plots of the TTFB-rotor system: (**a**) simulation results and (**b**) experimental results.

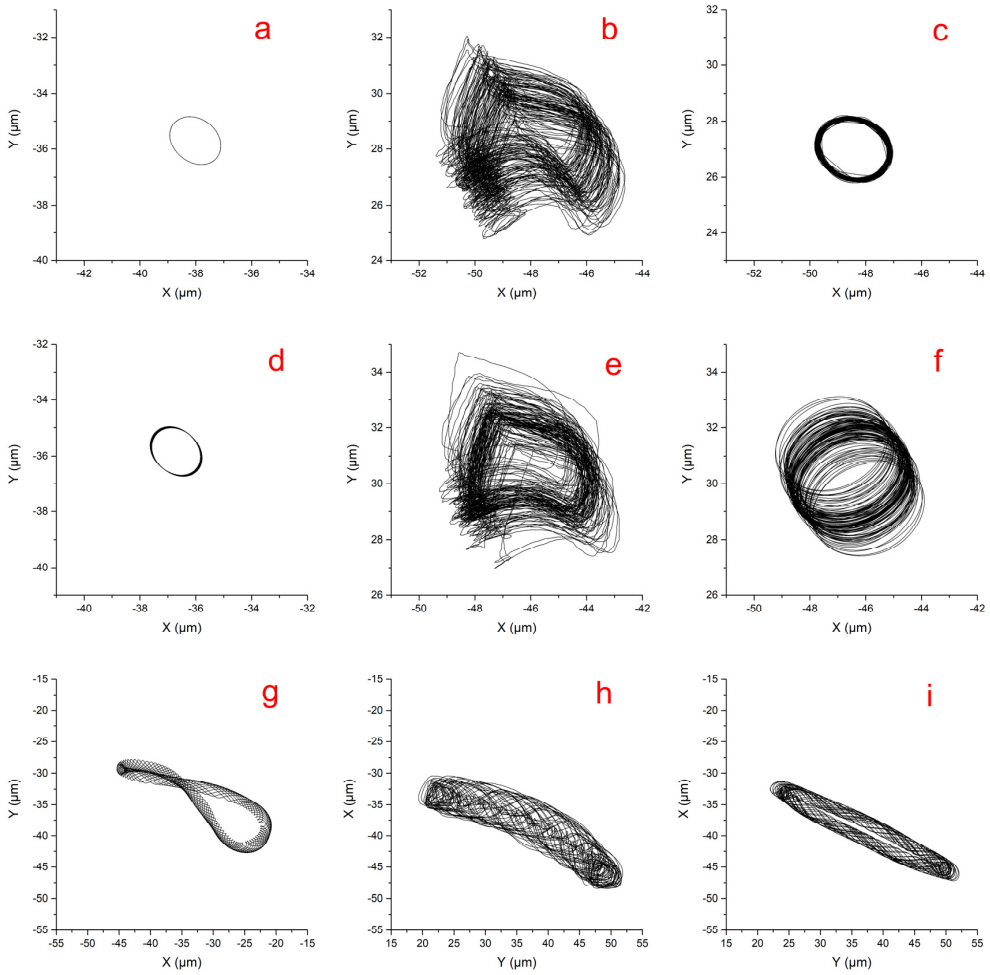

Figure 10. Orbits of rotor center at rotational speed of 24.6 krpm (**a**,**d**,**g**), 27 krpm (**b**,**e**,**h**), and 36 krpm (**c**,**f**,**i**). (**a**–**c**) Simulation results; (**d**–**f**) experimental results before filtering; and (**g**–**i**) experimental results after filtering.

To further validate the method, two additional cases were conducted with different bump foil stiffnesses. The first case involved a lower stiffness configuration, using a 0.1 mm C17200 bump foil material with a Young's modulus of 130 Gpa, resulting in 0.7 times the original stiffness as per the above model [27]. The second case utilized a higher stiffness configuration, using a 0.2 mm 3J1 alloy as the bump foil material with 8 times the original stiffness. Figure 11 illustrates waterfall plots depicting the simulation and experimental vertical vibrations at the right end. Upon comparing these plots, it is evident that even with variations in bump foil stiffness, the simulation results for synchronous and subsynchronous vibrations align well with the experimental results. The simulation's maximum stable speed and subsynchronous frequency also exhibit good agreement with the experimental findings. Thus, we can conclude that the time-domain orbit simulation accurately predicts the dynamic responses of TTFB-rotor systems.

The impact of bump foil stiffness on the dynamic responses of the TTFB-rotor system can also be inferred from these cases. It is observed that increasing the bump foil stiffness leads to a higher subsynchronous frequency. However, this observation contradicts the results of previous studies on GFB-rotor systems, which suggested a positive correlation between the subsynchronous frequency and the square root of bump foil stiffness [26]. This discrepancy implies that the thick top foil also plays a role in influencing the nonlinear responses of the TTFB-rotor system. Regarding the maximum stable speed, the simulation indicates that the maximum stable rotor speed for the lower bump stiffness bearing is 34.2 krpm, while the experimental result is 33.42 krpm. Similarly, for the original bearing,

the simulation and experimental results correspond to 36 krpm and 35.58 krpm, respectively. Finally, for the higher bump stiffness bearing, the simulation and experimental results show 39 krpm and 39.12 krpm. These findings clearly demonstrate that as the bump foil stiffness increases, the stable speed of the TTFB-rotor system also increases. Consequently, a TTFB-rotor system with a higher bump foil stiffness exhibits enhanced stability.

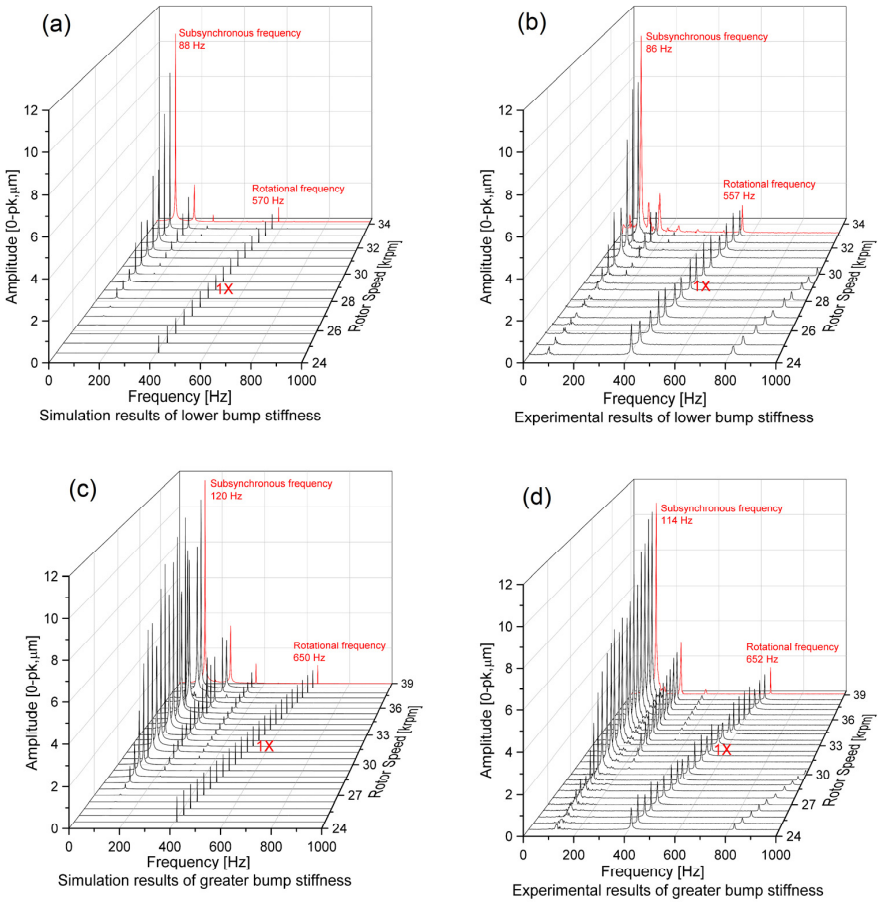

Figure 11. Waterfall plots of the TTFB-rotor system with different stiffness. (**a**) Simulation results of lower bump stiffness; (**b**) experimental results of lower bump stiffness; (**c**) simulation results of greater bump stiffness; and (**d**) experimental results of greater bump stiffness.

4. Parameter Studies and Discussion

In this section, we conduct parameter studies and discussions to examine the contributions of the gas film and shaft in the TTFB-rotor system. We investigate three key parameters: nominal clearance, static load, and unbalance. Through the use of waterfall plots, orbit simulations, Poincaré maps, and FFT plots, we present visual representations of the results obtained with varying parameters. These analyses reveal the respective influences of each parameter on the system's behavior.

4.1. Effects of Nominal Clearance

The gas film serves as a barrier between the bearing surface and the shaft, and it is responsible for generating dynamic pressure. The alteration of the nominal clearance directly affects the pressure distribution within the gas film. As a result, the nominal clearance exerts a significant influence on the stability of the TTFB-rotor system.

In this section, the system model considers the nominal clearance values of 40 μm, 50 μm, 70 μm, and 80 μm for each TTFB. The interval between the values is 10 μm, while all other conditions remain unchanged as previously described. Figure 12 illustrates the waterfall plots depicting the simulation responses for different nominal clearances. Additionally, in the previous section, the nominal clearance of 60 μm was studied and its corresponding

waterfall plot is displayed in Figure 9a. Comparing Figures 12 and 9a reveals that when the nominal clearance is less than 70 μm, the subsynchronous frequency decreases as the nominal clearance increases. However, once the nominal clearance exceeds 70 μm, the subsynchronous frequency remains constant, indicating that the pressure distribution in the high-pressure region of the gas film stabilizes beyond a specific nominal clearance. As a result, the subsynchronous frequency no longer varies. Regarding the maximum stable speed, as the nominal clearance increases from 40 μm to 80 μm, the maximum stable speed of the TTFB-rotor system increases from 19.2 krpm to 63.6 krpm. This implies that subsynchronous vibrations can be suppressed by increasing the nominal clearance. Moreover, greater nominal clearance enhances the stability of the TTFB-rotor system.

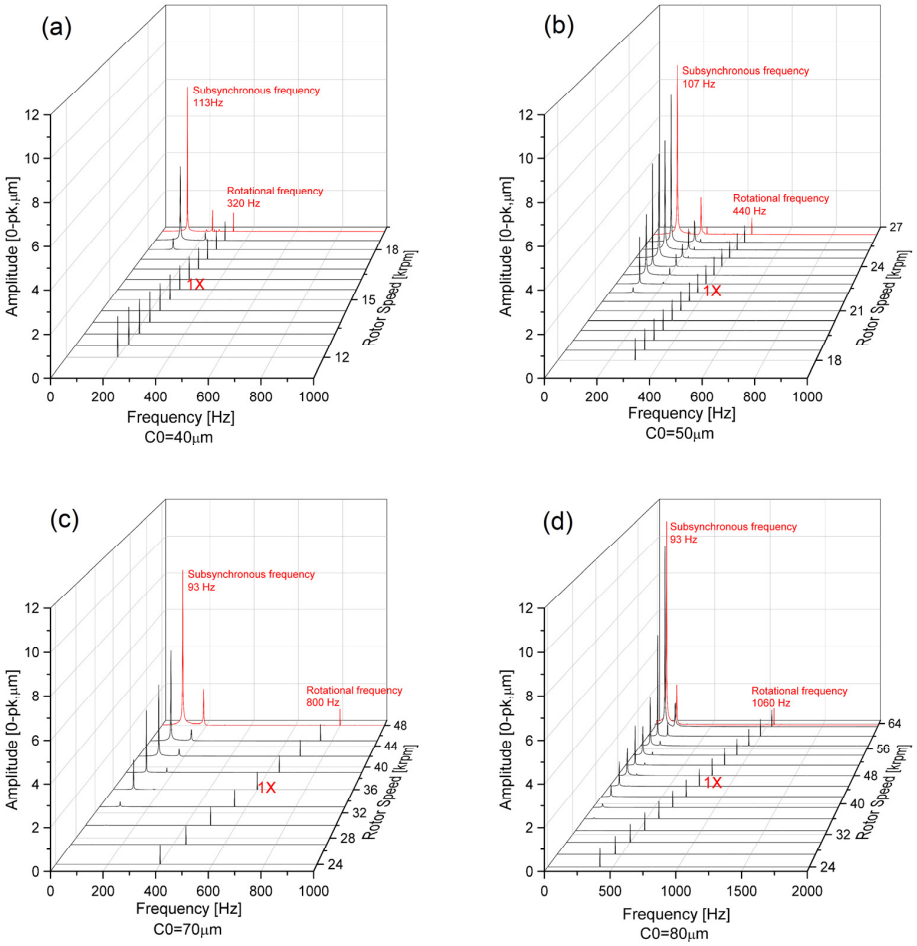

Figure 12. Waterfall plots of the TTFB-rotor system with various nominal clearances. (**a**) 40 μm; (**b**) 50 μm; (**c**) 70 μm; and (**d**) 80 μm.

The influencing mechanism of the nominal clearance on stability lies in its ability to alter the bearing attitude angle. As the nominal clearance increases, the film thickness in the high-pressure area decreases under the same static load. This results in an enlarged eccentricity ratio of the shaft and a reduction in the bearing attitude angle. The value of the bearing attitude angle represents the proportion of the tangential component of force acting on the shaft, with bearings featuring larger bearing attitude angles having smaller tangential component portions. The tangential component of force on the shaft typically injects energy into the rotor system, which is detrimental to its stable operation [30]. Consequently, increasing the nominal clearance improves the stability of the TTFB-rotor system.

4.2. Effects of Static Load

In order to further validate the influence of the bearing attitude angle on the stability of the TTFB-rotor system, this section examines the effects of static load. By increasing the

static load, the eccentricity ratio of the shaft can be amplified and the bearing attitude angle can be reduced for all foil bearings [31].

In this section, the system model utilizes static loads of 1.2 kg, 1.6 kg, 2.4 kg, and 2.8 kg for each TTFB. The interval between the static loads is 0.4 kg. As the static loads are changed by extra gravity coefficients, the structure of the rotor is not changed [26]. The other conditions remain unchanged as described previously. Figure 13 illustrates waterfall plots of simulation responses corresponding to different static loads. Additionally, the static load of 2.0 kg, examined in the previous section, with its corresponding waterfall plot is shown in Figure 9a. Combining Figures 9a and 12, it becomes apparent that as the bearing static load increases from 1.2 kg to 2.8 kg, the maximum stable speed of the TTFB-rotor system rises from 19.2 krpm to 54.6 krpm, accompanied by a slight enhancement in the subsynchronous frequency at the maximum stable speed. Figure 14 showcases the orbit simulations, Poincaré maps, and FFT plots of vertical vibrations for different static loads at a rotational speed of 27 krpm. For a static load of 1.6 kg, the orbit of the rotor center becomes complex, and the Poincaré map exhibits multiple distinct points forming two large regions. The rotor motion appears quasi-periodic, with significant subsynchronous frequency amplitude present in the FFT plot. As the static load increases, the amplitude of the subsynchronous frequency and the area enclosed by the distinct points in the Poincaré map gradually decrease. Beyond a static load of 2.0 kg, the quasiperiodic rotor motion transitions to a period-1 state, and the orbit of the rotor center becomes a simple circle. The FFT plot displays a single peak, indicating the elimination of the subsynchronous frequency. These results confirm that the reduction in the bearing attitude angle achieved by adding static load can suppress subsynchronous vibration and improve the stability of the TTFB-rotor system.

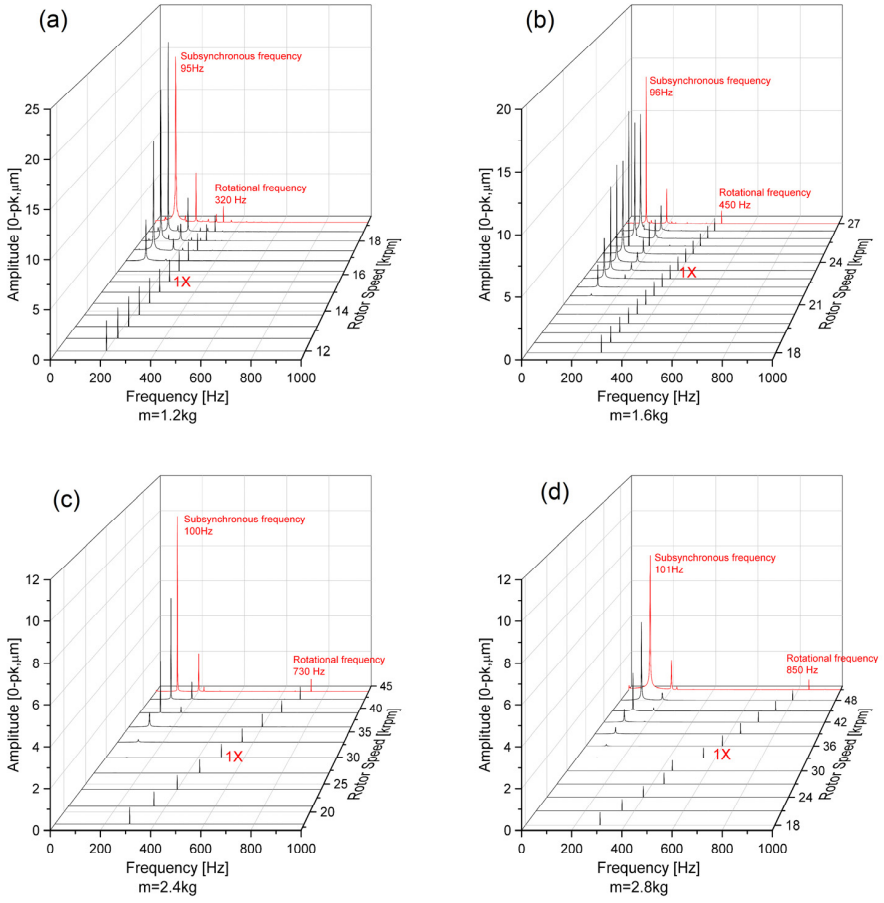

Figure 13. Waterfall plots of the TTFB-rotor system with various static loads. (**a**) 1.2 kg; (**b**) 1.6 kg; (**c**) 2.4 kg; and (**d**) 2.8 kg.

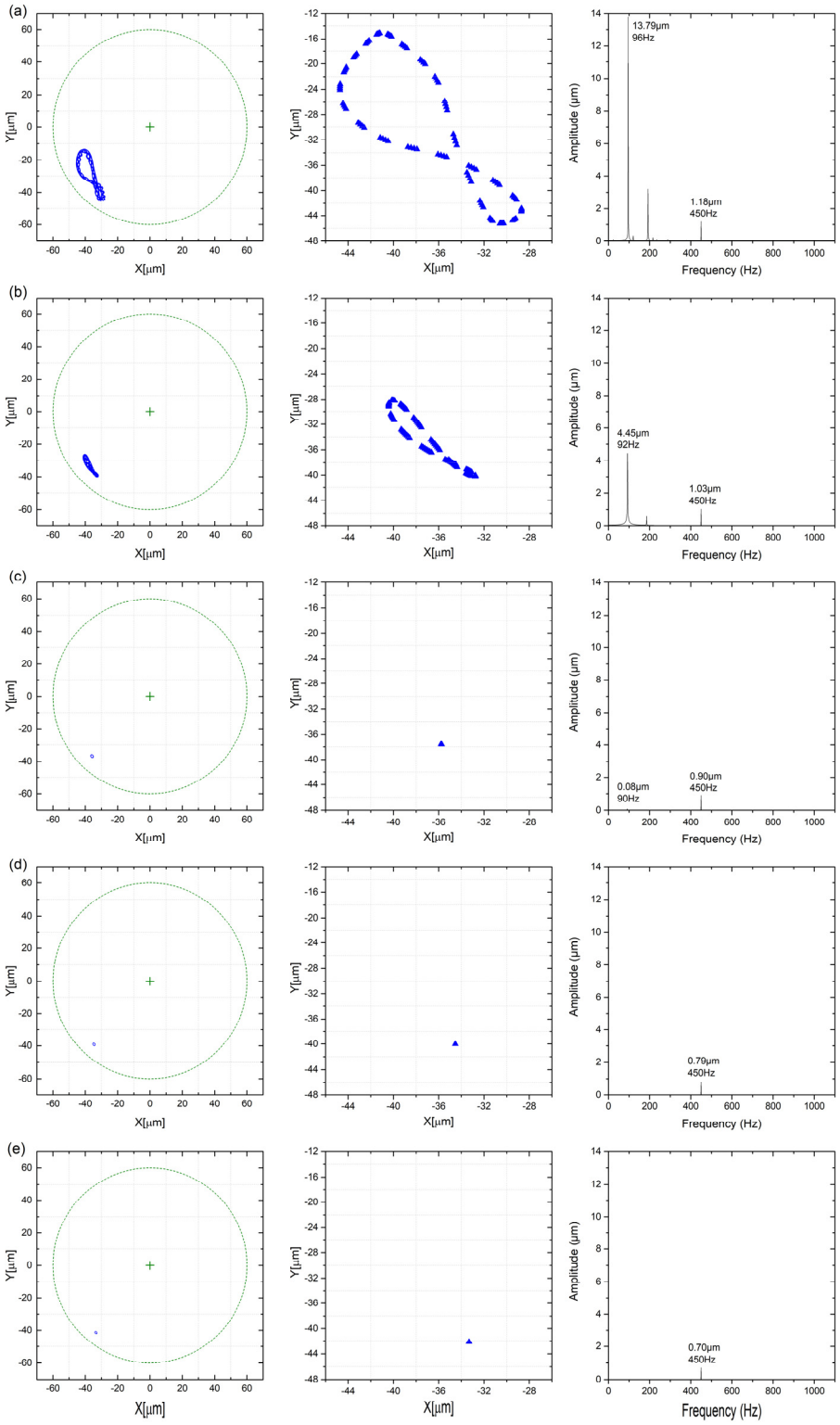

Figure 14. Orbit simulations, Poincaré maps, and FFT plots of vertical vibrations for different static loads at a rotational speed of 27 krpm. (**a**) m = 1.6 kg; (**b**) m = 1.8 kg; (**c**) m = 2.0 kg; (**d**) m = 2.2 kg; and (**e**) m = 2.4 kg.

4.3. Effects of Unbalance

Unbalance is a critical parameter that significantly influences the subsynchronous vibrations of GFB-rotor systems [20,21,32]. Therefore, this section discusses the effects of unbalance on TTFB-rotor systems. The unbalance values are set at 0 g·mm, 1 g·mm, 3 g·mm,

and 4 g·mm with an interval equaling half of the base unbalance. The base unbalance, which is 2 g·mm, is addressed in the simulation validation section. To prevent additional load caused by the phase difference in the unbalance, the two unbalanced masses are positioned axially in a symmetric manner, with identical angles.

Figure 15 illustrates the waterfall plots of simulation responses with various static loads. It can be observed that, similar to Figure 9a, all the systems have a maximum stable speed of 36 krpm, and their subsynchronous vibration amplitudes exhibit the same variation with speed. On the other hand, Figure 16 presents the orbit simulations, Poincaré maps, and FFT plots of vertical vibrations for different unbalances at a rotational speed of 36 krpm. The orbits of the rotor center are highly intricate for all cases, mostly showing quasiperiodic motion with multiple distinct points in the Poincaré maps. Notably, when the unbalance is 3 g·mm, the orbit displays an interesting shape, transitioning the rotor center motion to a period-6 pattern, as the subsynchronous frequency precisely equals 1/6 of the rotational frequency. Additionally, in the FFT plots, the synchronous vibration amplitude increases with unbalance yet remains significantly smaller than the subsynchronous frequency amplitude. As depicted in Figure 17, there is a strong positive correlation (correlation coefficient of 0.9998) between the synchronous vibration amplitude and the unbalance. These findings imply that unbalance influences synchronous vibration but has minimal impact on subsynchronous vibration. This is in contrast with previous studies on GFB-rotor systems [20,21,32]. Consequently, for engineering applications utilizing TTFBs, extreme balancing of the rotor is unnecessary and of little significance.

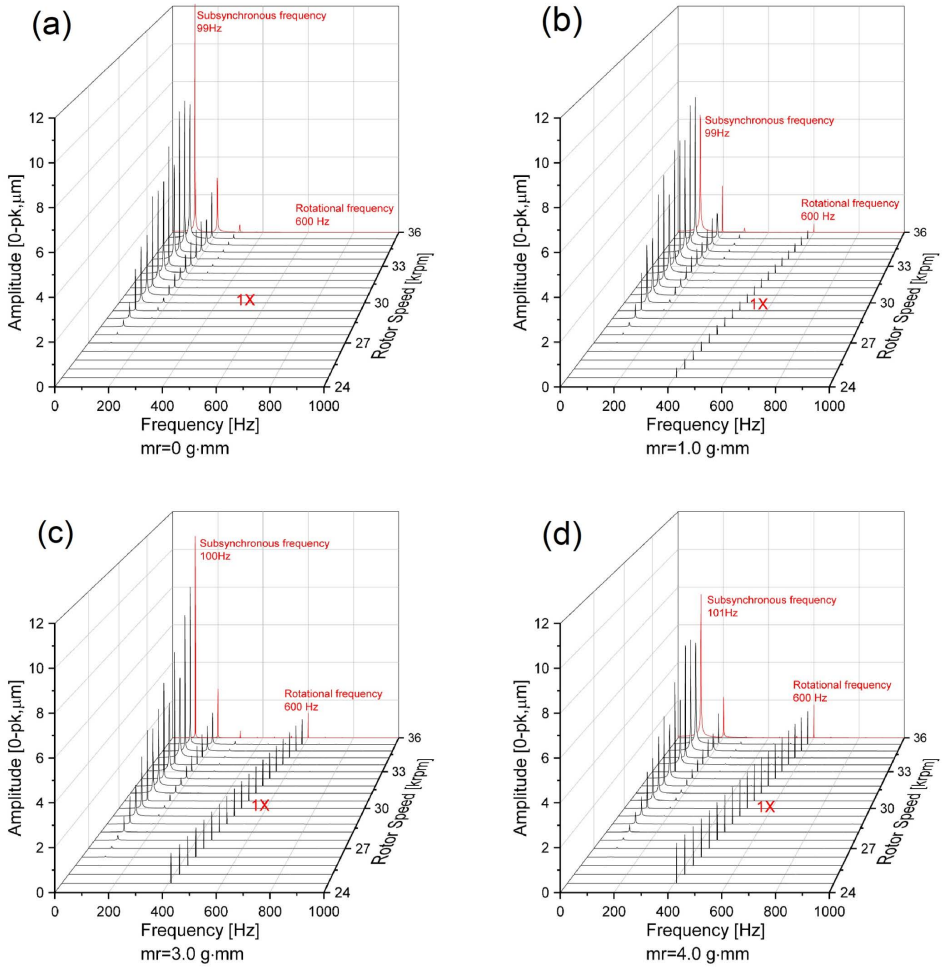

Figure 15. Waterfall plots of the TTFB-rotor system with various unbalances. (**a**) 0 g·mm; (**b**) 1 g·mm; (**c**) 3 g·mm; and (**d**) 4 g·mm.

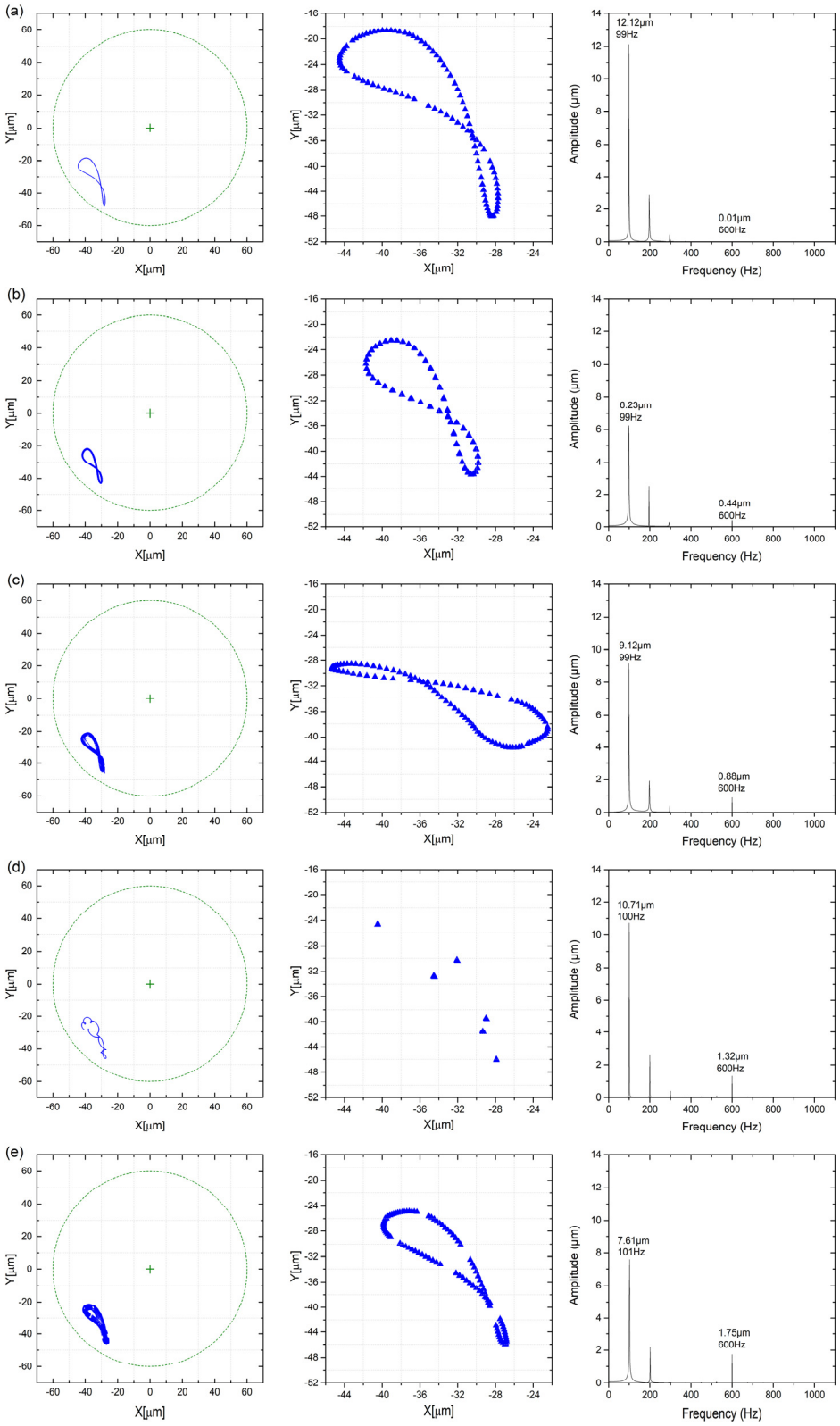

Figure 16. Orbit simulations, Poincaré maps, and FFT plots of vertical vibrations for different unbalances of the maximum stable speed. (**a**) mr = 0 g·mm; (**b**) mr = 1 g·mm; (**c**) mr = 2 g·mm; (**d**) mr = 3 g·mm; and (**e**) mr = 4 g·mm.

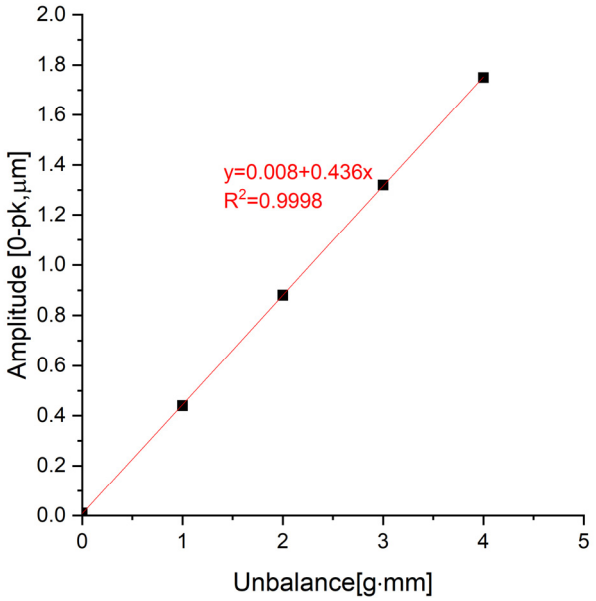

Figure 17. Synchronous vibration amplitude of various unbalances.

5. Conclusions

In this study, we developed a nonlinear dynamic model for TTFB-rotor systems by combining unsteady Reynolds equations, foil deformation equations, thick top foil motion equations, and rotor motion equations. This comprehensive model enables us to predict the dynamic responses of the TTFB-rotor system using time-domain orbit simulations, which accurately determine the rotor's orbital path.

To validate the accuracy of our model, we constructed a symmetrical test rig that effectively minimizes errors caused by varying bearing loads. We conducted calculations and tests using three different types of TTFBs with varying bump foil stiffness. The resulting waterfall plots of vibrations, both calculated and tested, indicated that higher bump foil stiffness effectively suppresses subsynchronous vibrations. Furthermore, by comparing these simulation results with the corresponding experimental results, we observed a strong correlation in vibration patterns, validating the reliability of our model.

Based on our new model, we conducted separate studies on the effects of nominal clearance, static load, and unbalance on the TTFB-rotor system. It was found that increasing the nominal clearance or the static load, both of which reduce the bearing attitude angle, enhances the maximum stable speed of the TTFB-rotor system. As a result, for TTFB-rotor systems, other related parameters reducing the bearing attitude angle contribute to improved stability. In terms of unbalance, it was observed that an increase in unbalance has a strong positive correlation with the amplitude of synchronous vibration. However, unbalance has minimal impact on subsynchronous vibrations, and all TTFB-rotor systems exhibit the same maximum stable speed. This study not only demonstrates an advanced tool for predicting the dynamic responses of TTFB-rotor systems but also paves the way for future developments of TTFB in high-speed rotating machinery systems.

Author Contributions: Conceptualization, B.H. and A.H.; methodology, B.H.; software, B.H. and X.Y.; validation, B.H. and R.W.; formal analysis, B.H.; investigation, B.H.; data curation, B.H.; writing—original draft preparation, B.H.; writing—review and editing, X.Y. and Z.W.; resources, Q.N. and Z.L.; visualization, B.H.; supervision, A.H.; funding acquisition, A.H. All authors have read and agreed to the published version of the manuscript.

Funding: This research was funded by the National Science and Technology Major Project of China, grant number J2019-V-0017-0112.

Data Availability Statement: The data presented in this study are available on reasonable request from the corresponding author.

Conflicts of Interest: Author Qifeng Ni was employed by the company Ningbo Hudu Energy Technology Co., Ltd. The remaining authors declare that the research was conducted in the absence of any commercial or financial relationships that could be construed as a potential conflict of interest.

References

1. DellaCorte, C.; Radil, K.C.; Bruckner, R.J.; Howard, S.A. Design, Fabrication, and Performance of Open Source Generation I and II Compliant Hydrodynamic Gas Foil Bearings. *Tribol. Trans.* **2008**, *51*, 254–264. [CrossRef]
2. Somaya, K.; Yamashita, T.; Yoshimoto, S. Experimental and Numerical Investigation of the High-Speed Instability of Aerodynamic Foil Journal Bearings for Micro Turbomachinery. In Proceedings of the ASME/STLE 2012 International Joint Tribology Conference, Denver, CO, USA, 7–10 October 2012; pp. 243–245.
3. Samanta, P.; Murmu, N.C.; Khonsari, M.M. The evolution of foil bearing technology. *Tribol. Int.* **2019**, *135*, 305–323. [CrossRef]
4. Heshmat, H.; Walowit, J.A.; Pinkus, O. Analysis of Gas-Lubricated Foil Journal Bearings. *J. Lubr. Technol.* **1983**, *105*, 647–655. [CrossRef]
5. DellaCorte, C. Oil-Free shaft support system rotordynamics: Past, present and future challenges and opportunities. *Mech. Syst. Signal Process.* **2012**, *29*, 67–76. [CrossRef]
6. Xiong, L.Y.; Wu, G.; Hou, Y.; Liu, L.Q.; Ling, M.F.; Chen, C.Z. Development of aerodynamic foil journal bearings for a high speed cryogenic turboexpander. *Cryogenics* **1997**, *37*, 221–230. [CrossRef]
7. Hou, Y.; Zhu, Z.H.; Chen, C.Z. Comparative test on two kinds of new compliant foil bearing for small cryogenic turbo-expander. *Cryogenics* **2004**, *44*, 69–72. [CrossRef]
8. Lee, Y.-B.; Kwak, Y.-S.; Chung, J.T.; Sim, K. Microturbocharger with Air Foil Bearings for a 100-W Class Micro Power System and Improvement of Rotordynamic Performance. *Tribol. Trans.* **2011**, *54*, 939–948. [CrossRef]
9. DellaCorte, C.; Bruckner, R.J. Remaining Technical Challenges and Future Plans for Oil-Free Turbomachinery. *J. Eng. Gas Turbines Power* **2010**, *133*, 042502. [CrossRef]
10. Guan, H.-Q.; Feng, K.; Yu, K.; Cao, Y.-L.; Wu, Y.-H. Nonlinear dynamic responses of a rigid rotor supported by active bump-type foil bearings. *Nonlinear Dyn.* **2020**, *100*, 2241–2264. [CrossRef]
11. Ku, C.P.R.; Heshmat, H. Structural Stiffness and Coulomb Damping in Compliant Foil Journal Bearings: Theoretical Considerations. *Tribol. Trans.* **1994**, *37*, 525–533. [CrossRef]
12. Lee, Y.B.; Kim, T.H.; Kim, C.H.; Lee, N.S.; Choi, D.H. Unbalance Response of a Super-Critical Rotor Supported by Foil Bearings—Comparison with Test Results©. *Tribol. Trans.* **2004**, *47*, 54–60. [CrossRef]
13. Vleugels, P.; Waumans, T.; Peirs, J.; Al-Bender, F.; Reynaerts, D. High-speed bearings for micro gas turbines: Stability analysis of foil bearings. *J. Micromech. Microeng.* **2006**, *16*, S282–S289. [CrossRef]
14. Kim, T.H.; Andrés, L.S. Effects of a Mechanical Preload on the Dynamic Force Response of Gas Foil Bearings: Measurements and Model Predictions. *Tribol. Trans.* **2009**, *52*, 569–580. [CrossRef]
15. Fangcheng, X.; Daejong, K. Dynamic performance of foil bearings with a quadratic stiffness model. *Neurocomputing* **2016**, *216*, 666–671. [CrossRef]
16. Hoffmann, R.; Liebich, R. Characterisation and calculation of nonlinear vibrations in gas foil bearing systems—An experimental and numerical investigation. *J. Sound Vib.* **2018**, *412*, 389–409. [CrossRef]
17. Kim, D. Parametric Studies on Static and Dynamic Performance of Air Foil Bearings with Different Top Foil Geometries and Bump Stiffness Distributions. *J. Tribol.* **2007**, *129*, 354–364. [CrossRef]
18. Bou-Saïd, B.; Grau, G.; Iordanoff, I. On Nonlinear Rotor Dynamic Effects of Aerodynamic Bearings with simple flexible rotors. *J. Eng. Gas Turbines Power* **2007**, *130*, 012503. [CrossRef]
19. Larsen, J.S.; Santos, I.F.; von Osmanski, S. Stability of rigid rotors supported by air foil bearings: Comparison of two fundamental approaches. *J. Sound Vib.* **2016**, *381*, 179–191. [CrossRef]
20. Bhore, S.P.; Darpe, A.K. Nonlinear dynamics of flexible rotor supported on the gas foil journal bearings. *J. Sound Vib.* **2013**, *332*, 5135–5150. [CrossRef]
21. Larsen, J.S.; Santos, I.F. On the nonlinear steady-state response of rigid rotors supported by air foil bearings—Theory and experiments. *J. Sound Vib.* **2015**, *346*, 284–297. [CrossRef]
22. von Osmanski, S.; Larsen, J.S.; Santos, I.F. A fully coupled air foil bearing model considering friction—Theory & experiment. *J. Sound Vib.* **2017**, *400*, 660–679. [CrossRef]
23. Bonello, P.; Hassan, M.F.B. An experimental and theoretical analysis of a foil-air bearing rotor system. *J. Sound Vib.* **2018**, *413*, 395–420. [CrossRef]
24. Wang, R.; Hou, A.; Li, Z. Numerical investigation of gas journal foil bearing performance with thick top foil. *J. Aerosp. Power* **2020**, *35*, 2123–2135. (In Chinese) [CrossRef]
25. Li, J.; Li, C.; Du, J. Investigations of the Bump Foil Bearing With Thick Top Foil Based on Contact Mechanics. *J. Tribol.* **2023**, *145*, 074601. [CrossRef]
26. Guo, Z.; Feng, K.; Liu, T.; Lyu, P.; Zhang, T. Nonlinear dynamic analysis of rigid rotor supported by gas foil bearings: Effects of gas film and foil structure on subsynchronous vibrations. *Mech. Syst. Signal Process.* **2018**, *107*, 549–566. [CrossRef]
27. Iordanoff, I. Analysis of an Aerodynamic Compliant Foil Thrust Bearing: Method for a Rapid Design. *J. Tribol.* **1999**, *121*, 816–822. [CrossRef]

28. Zhang, G.-h.; Sun, Y.; Liu, Z.-s.; Zhang, M.; Yan, J.-j. Dynamic characteristics of self-acting gas bearing–flexible rotor coupling system based on the forecasting orbit method. *Nonlinear Dyn.* **2012**, *69*, 341–355. [CrossRef]
29. Oppenheim, A.V.; Schafer, R.W.; Buck, J.R. *Discrete-Time Signal Processing*, 2nd ed.; Prentice-Hall, Inc.: Upper Saddle River, NJ, USA, 1999; pp. 237–240.
30. Edgar, J.; Gunter, J. *Dynamic Stability of Rotor-Bearing Systems*; National Aeronautics and Space Administration: Cleveland, OH, USA, 1966; Volume NASA SP-113, p. 228.
31. Lee, D.-H.; Kim, Y.-C.; Kim, K.-W. The effect of Coulomb friction on the static performance of foil journal bearings. *Tribol. Int.* **2010**, *43*, 1065–1072. [CrossRef]
32. Andrés, L.S.; Kim, T.H. Forced nonlinear response of gas foil bearing supported rotors. *Tribol. Int.* **2008**, *41*, 704–715. [CrossRef]